




Boids in a loop: Self-propelled particles within a flexible boundaryA. C. Quillen ^{1,*}, J. P. Smucker ^{1,2,†} and A. Peshkov ^{1,‡}¹*Department of Physics and Astronomy, University of Rochester, Rochester, New York 14618, USA*²*Department of Physics, Pennsylvania State University, Behrend, Pennsylvania 16513, USA*

(Received 4 February 2020; accepted 9 April 2020; published 27 May 2020)

We numerically explore the behavior of repelling and aligning self-propelled polar particles (boids) in two dimensions enclosed by a damped flexible and elastic loop-shaped boundary. We observe disordered, polar ordered, jammed, and circulating states. The latter produce a rich variety of boundary shapes, including circles, ovals, irregulars, ruffles, or sprockets, depending upon the bending moment of the boundary and the boundary to particle mass ratio. With the exception of the circulating states with nonround boundaries, states resemble those exhibited by attracting self-propelled particles, but here the confining boundary acts in place of a cohesive force. We attribute the formation of ruffles to instability mediated by pressure on the boundary when the speed of waves on the boundary approximately matches the self-propelled particle's swim speed.

DOI: [10.1103/PhysRevE.101.052618](https://doi.org/10.1103/PhysRevE.101.052618)**I. INTRODUCTION**

Active systems are nonequilibrium collections of self-propelled particles that exhibit a number of striking patterns including flocking, spontaneous aggregation, and formation of vortex or ringlike collective motion (e.g., Refs. [1–7]). Inspired by biological systems exhibiting collective phenomena such as flocking [8], artificial systems have been designed [9–12] that inject energy at the microscopic level and emulate the unique properties of their biological counterparts.

Collective behaviors can also emerge in confined geometries due to interactions with the boundary or the surrounding fluid (e.g., Refs. [12–14]). Confining walls may promote the creation of microscale patterns, for example, wavelike cell migration modes [15]. Active particles can interact collectively with movable rigid or flexible objects. For example, the fluctuations in active medium can affect the folding configurations of a flexible polymer [16] while the self-propulsion energy can be harnessed to power microscopic rotating gears [17,18]. Boundaries can be incorporated into the design of active matter based devices, for example, to generate fluid flow from confined bacteria [19]. For a review of active particles in crowded environments, see Ref. [20]. We focus here on self-propelled particles that are confined by a flexible loop-shaped boundary (e.g., Refs. [21–25]).

Soft boundaries, including loops, membranes, thin elastic rods, and plates, are interesting potential components for design. Pressure exerted by the active units can drive immersed objects to move directionally [18,26]. Soft boundaries can influence collective motion in active matter due to the “swim pressure” exerted by the particles on a boundary [22,27–29]. Flexible materials can dynamically respond with more degrees of freedom than rigid bodies such as walls, wedges,

or ratchets. Such systems may have practical applications in microbiomechanics, where flexible synthetic autonomous mechanisms can be used as drug-delivery agents, as passible cargo transport, or for mechanical actuation, as suggested by Paoluzzi *et al.* [23].

In this study, we numerically explore the behavior of self-propelled particles in two dimensions (2D) that are enclosed within a flexible circular boundary. We search for forms of collective behavior involving motions in the boundary, such as ovals or dumbbell shapes [23,25], or wavelike instabilities on the boundary [22]. We are interested in complex interactions between the particles and the boundary that can lead to new types of artificial mechanisms that harness collective motion.

We work with the class of dry aligning dilute active matter, which is called DADAM (see Ref. [30]). Discrete time polar self-propelled particle models [1,2] come in deterministic or stochastic varieties (e.g., Refs. [4,30–34]) and the self-propelled particles within them are sometimes called “boids,” following Reynolds [1]. We focus here on the deterministic variety. Our study is most similar to the numerical work by Nikola *et al.* [22], Paoluzzi *et al.* [23], and Wang *et al.* [25] and experimental study of vibrating robotic rods by Deblais *et al.* [24], who also studied repulsive active particles in two dimensions that interact with a flexible boundary. However, our simulations lack stochastic perturbations and particles within our simulations align their direction of motion with the direction of nearby particles, as in simulations of flocking (e.g., Refs. [1,2,4,32]). Prior simulations of self-propelled particles within a flexible loop have focused on nonaligning self-propelled particles with stochastically perturbed directions of motion (e.g., Refs. [23,25]).

In Sec. II, we describe our numerical model of self-propelled particles that are enclosed inside a flexible boundary. In Sec. III, we illustrate the phenomena seen with our simulations and discuss collective behavior and the nature of instability on the boundary. Summary and discussion follow in Sec. IV. Additional details for the numerical model are included in the Appendix.

*alice.quillen@rochester.edu

†jps45@psu.edu

‡apeshkov@ur.rochester.edu

II. BOID AND BOUNDARY MODEL

We adopt a simplified model with pointlike particles whose dynamics is described with effective forces [35]. This is in contrast with a more fine-grained model where the particle shape, the self-propulsion mechanism, the internal degrees of freedom of microswimmers, and the hydrodynamics interactions are also modeled (e.g., Refs. [13,14]).

Our two-dimensional model has two particle components, a boundary that is composed of discrete mass nodes, and a flock of self-propelled particles or boids. Both boundary nodes and boids have mass and can move. We describe in detail our numerical implementation as it contains more degrees of freedom than simulations of unconfined self-propelled particles (e.g., Ref. [32]) or self-propelled particles with periodic boundary conditions (e.g., Ref. [36]).

Both boundary nodes and boids can move and are massive; however, boundary nodes remain in a linear chain. The coordinates are in two dimensions only. The flexible boundary is initially a circular loop and encloses the boids.

We first discuss the numerical description of the flock of boids (Sec. II A), then the boundary (Sec. II B), and finally the interactions between boids and boundary (Sec. II C). Additional details on our numerical implementation can be found in the Appendix. Initial conditions are described in the Appendix, Subsec. A 1. The units and constraints on the time step are discussed in Subsecs. A 2 and A 3. Additional restrictions on parameter choices are discussed in Subsec. A 5. The code repositories are given in Subsec. A 6.

A. The flock of boids

A boid particle with index i has position \mathbf{x}_i^n at time denoted with index n . The particle velocity at the same time is \mathbf{v}_i^n and its mass is m_{boid} . The total number of boids is N_{boids} and the total mass in boids is $M_{\text{boids}} = N_{\text{boids}}m_{\text{boid}}$. We update boid positions and velocities using the first order (in time) Eulerian method (as in Ref. [31]) and with a fixed time step dt

$$\mathbf{x}_i^{n+1} = \mathbf{x}_i^n + \mathbf{v}_i^n dt, \quad (1)$$

$$\mathbf{v}_i^{n+1} = \mathbf{v}_i^n + \frac{dt}{m_{\text{boid}}} \mathbf{F}_{\text{boid},i}^n, \quad (2)$$

$$\mathbf{F}_{\text{boid},i}^n = \mathbf{F}_{\text{align},i}^n + \mathbf{F}_{\text{repel},i}^n + \mathbf{F}_{\text{interact},i}^n, \quad (3)$$

where $\mathbf{F}_{\text{boid},i}^n$ is a sum of forces that depend on boid position and velocity ($\mathbf{x}_i^n, \mathbf{v}_i^n$), neighboring boid positions and velocities ($\mathbf{x}_j^n, \mathbf{v}_j^n$ with $j \neq i$), and nearby boundary node positions. Hereafter, we will often omit the superscript n . It is useful to define a vector between two particle positions $\mathbf{r}_{i,j} \equiv \mathbf{x}_i - \mathbf{x}_j$, its length $r_{i,j} = |\mathbf{r}_{i,j}|$, and direction indicated by the unit vector $\hat{\mathbf{r}}_{i,j} = \mathbf{r}_{i,j}/r_{i,j}$. Here we use $\mathbf{r}_{i,j}$ for the vector between two boid positions but below we will also use $\mathbf{r}_{i,j}$ to describe the vector between two node positions and the vector between a node and a boid position.

For our self-propelled particles, we employ a Vicsek type of model [2], causing nearby particles to align, but we lack stochastic perturbations that would change the direction of motion. We include an additional interboid repelling force (e.g., as used by Refs. [4,22,23,25,32,33]) but no interboid attractive or cohesive forces.

The repel force on boid with index i is a sum over repulsion forces from nearby boids with index j

$$\mathbf{F}_{\text{repel},i} = \sum_{i \neq j, r_{i,j} < 2d_{\text{repel}}} \frac{m_{\text{boid}} U_{\text{repel}}}{d_{\text{repel}}} e^{-r_{i,j}/d_{\text{repel}}} \hat{\mathbf{r}}_{i,j}. \quad (4)$$

Here U_{repel} has units of the square of velocity and d_{repel} characterizes the scale of the repulsive interaction. We only apply the repel force for boid pairs separated by $r_{i,j} < 2d_{\text{repel}}$. The repel force is applied equally and oppositely to boid pairs. This repel force is exponential (as was that adopted by Ref. [32]). We also explored a repel force inversely proportional to the interboid distance and saw similar collective phenomena.

The alignment force also serves to propel the boids at a speed that is approximately v_0 . The align or steer and self-propelling force exerted on boid i is

$$\mathbf{F}_{\text{align},i} = \alpha_{\text{align}} m_{\text{boid}} (v_0 \hat{\mathbf{w}}_i - \mathbf{v}_i), \quad (5)$$

$$\hat{\mathbf{w}}_i = \frac{\mathbf{w}_i}{|\mathbf{w}_i|}. \quad (6)$$

Here α_{align} has units of inverse time and v_0 is the boid speed, equal to the ‘‘terminal velocity’’ in the model by Touma *et al.* [32]. The unit vector $\hat{\mathbf{w}}_i$ is multiplied by v_0 so that the boid accelerates if its speed is slower than v_0 and it decelerates if it is going faster than v_0 . A distance d_{align} characterizes the scale of the alignment interactions. A boid lacking neighbors that are within alignment distance d_{align} is propelled using the boid’s own current velocity direction with $\mathbf{w}_i = \mathbf{v}_i$. For a boid with near neighbors, the vector \mathbf{w}_i is computed from the velocities of nearby boids, similar to prior numerical models [2,4],

$$\mathbf{w}_i = \sum_{i \neq j, r_{i,j} < d_{\text{align}}} \mathbf{v}_j. \quad (7)$$

B. The flexible elastic boundary

The numerical description of our flexible boundary is similar to that used by Nikola *et al.* [22] (see VI of their supplements). The boundary is described with a chain of mass nodes, each of mass m_{node} . Each node is separated from its two nearest neighbors by a spring with rest length Δs . The chain is closed by connecting its two endpoints so that it forms a loop. A node at position \mathbf{y}_i has neighbors \mathbf{y}_{i+1} and \mathbf{y}_{i-1} with indices given modulo the total number of nodes in the chain, N_{nodes} . The total mass in the boundary is $M_{\text{nodes}} = N_{\text{nodes}}m_{\text{node}}$. The springs maintain the boundary length and have rest length $\Delta s = 2\pi R/N_{\text{nodes}}$, where R is the initial loop radius. To resist bending, we apply forces to the nodes using a thin elastic beam approximation.

We update node positions and velocities using equations similar to Eqs. (1) and (2):

$$\mathbf{y}_i^{n+1} = \mathbf{y}_i^n + \mathbf{u}_i^n dt, \quad (8)$$

$$\mathbf{u}_i^{n+1} = \mathbf{u}_i^n + \frac{dt}{m_{\text{node}}} \mathbf{F}_{\text{node},i}^n. \quad (9)$$

Instead of Eq. (3), the sum of forces on node i at time step n is

$$\mathbf{F}_{\text{node},i}^n = \mathbf{F}_{\text{bend},i}^n + \mathbf{F}_{\text{spring},i}^n + \mathbf{F}_{\text{interact},i}^n + \mathbf{F}_{\text{damp},i}^n. \quad (10)$$

These forces depend on node position and velocity ($\mathbf{y}_i^n, \mathbf{u}_i^n$), neighboring node positions and velocities ($\mathbf{y}_j^n, \mathbf{u}_j^n$ with $j \neq i$), and positions of nearby boids (\mathbf{x}_k^n with index k specifying boids that are nearby). We first discuss the bending forces and then the spring forces.

For the bending force, we use the Euler-Bernoulli theory of thin elastic beams. The centerline of a beam is described with a curve $\mathbf{X}(s)$ where ds gives length along the boundary. The elastic potential energy depends on

$$U_{\text{bend}} = \int ds \frac{\alpha_{\text{bend}}}{2} [\mathbf{X}''(s)]^2, \quad (11)$$

where $\mathbf{X}'' = \frac{\partial^2 \mathbf{X}(s)}{\partial s^2}$ is the curvature. The coefficient $\alpha_{\text{bend}} = EI$, is known as the bending moment or flexural rigidity, with E being the elastic modulus and I being the beam cross section's integrated second moment of area.

For a linear beam oriented on the x axis with linear mass density μ , and displacement from the x axis $w(x, t)$, the above potential energy gives equation of motion

$$\mu \frac{\partial^2 w}{\partial t^2} = -\alpha_{\text{bend}} \frac{\partial^4 w}{\partial x^4}. \quad (12)$$

We discretize our boundary by putting its mass into a consecutive set of mass nodes \mathbf{y}_i , each separated by distance Δs and of equal mass. The curvature at a node

$$\mathbf{y}_i'' \approx (\Delta s)^{-2} (\mathbf{y}_{i+1} + \mathbf{y}_{i-1} - 2\mathbf{y}_i). \quad (13)$$

The potential energy for the discrete chain

$$U_{\text{bend}} = \sum_i \frac{\alpha_{\text{bend}}}{(\Delta s)^3} (3|\mathbf{y}_i|^2 + \mathbf{y}_i \cdot \mathbf{y}_{i+2} - 4\mathbf{y}_i \cdot \mathbf{y}_{i+1}). \quad (14)$$

Taking the derivative of potential energy U_{bend} with respect to node position \mathbf{y}_i gives the force on a node

$$\begin{aligned} \mathbf{F}_{\text{bend},i} &= -\frac{\partial U_{\text{bend}}}{\partial \mathbf{y}_i} \\ &= -\frac{\alpha_{\text{bend}}}{(\Delta s)^3} (\mathbf{y}_{i-2} - 4\mathbf{y}_{i-1} + 6\mathbf{y}_i - 4\mathbf{y}_{i+1} + \mathbf{y}_{i+2}). \end{aligned} \quad (15)$$

The equation of motion

$$m_{\text{node}} \frac{d^2 \mathbf{y}_i}{dt^2} = -\frac{\alpha_{\text{bend}}}{(\Delta s)^3} (\mathbf{y}_{i-2} - 4\mathbf{y}_{i-1} + 6\mathbf{y}_i - 4\mathbf{y}_{i+1} + \mathbf{y}_{i+2}) \quad (16)$$

is a discrete approximation to the equation of motion from Euler-Bernoulli elastic beam theory (e.g., Refs. [37,38]).

We insert a spring between each consecutive node on the boundary. The springs are intended to maintain a nearly constant length boundary. The total potential energy due to springs is

$$U_{\text{spring}} = \sum_i \frac{k_s}{2} (r_{i,i-1} - \Delta s)^2 \quad (17)$$

where $r_{i,i-1} = |\mathbf{y}_i - \mathbf{y}_{i-1}|$ is the distance between two consecutive nodes, Δs is the rest spring length, and k_s is the spring constant. The force exerted on each node due to the

TABLE I. Common parameters for simulation series.

N_{nodes}	150
$\alpha_{\text{align}} t_R$	3
$\gamma_{\text{damp}} t_R$	0.1
$k_s m_{\text{node}}^{-1} t_R^2$	2×10^4
$F_{\text{interact}} M_{\text{boids}}^{-1} v_0^{-2} R$	1.5
d_{interact}/R	0.02
dt/t_R	0.005
t_{max}/t_R	50
ϵ_{ks}	0.03

The time t_R is defined in Eq. (A1). The parameter ϵ_{ks} is defined in Eq. (A8).

springs is

$$\begin{aligned} \mathbf{F}_{\text{spring},i} &= -k_s \frac{(\mathbf{y}_i - \mathbf{y}_{i-1})}{r_{i,i-1}} (r_{i,i-1} - \Delta s) \\ &\quad - k_s \frac{(\mathbf{y}_i - \mathbf{y}_{i+1})}{r_{i,i+1}} (r_{i,i+1} - \Delta s). \end{aligned} \quad (18)$$

This follows common implementations of N -body mass-spring models (e.g., Ref. [39]).

To mimic an external viscous or friction-like boundary interaction, we add a velocity-dependent damping force on each boundary node

$$\mathbf{F}_{\text{damp},i} = -m_{\text{node}} \gamma_{\text{damp}} \mathbf{u}_i, \quad (19)$$

where damping parameter γ_{damp} is in units of inverse time and \mathbf{u}_i is velocity of the node.

C. Boundary node/boid interactions

We apply an equal and opposite repulsive force to each pair of boundary and boid particles. The force on particle i (either a boundary node or boid) from particle with index j (of the opposite type) is given by

$$\mathbf{F}_{\text{interact},i} = \sum_{j, r_{i,j} < 3d_{\text{interact}}} F_{\text{interact}} e^{-r_{i,j}/d_{\text{interact}}} \hat{\mathbf{r}}_{i,j}. \quad (20)$$

Here $r_{i,j}$ is the distance between the node and boid and $\hat{\mathbf{r}}_{i,j}$ is a unit vector pointing from one particle to the other. The distance d_{interact} describes the range of the interaction. We only apply the force at distances $r_{i,j} < 3d_{\text{interact}}$. The parameter F_{interact} determines the strength of the interaction. As long as the interaction force causes accelerations that exceed those from other forces and so causes reflection off the boundary faster than interboid distance travel times, the collective behavior should not be sensitive to d_{interact} or F_{interact} .

III. COLLECTIVE PHENOMENA

In Fig. 1, each row shows a series of 11 simulations. Each panel is a simulation snap shot that shows the boid distribution and boundary morphology at the end of a simulation. Boundary particles are shown in red. Each boid is marked with a navy blue isosceles triangle. The vertex with narrowest angle marks the direction of motion. In each simulation series, parameters are identical except for one parameter, which is

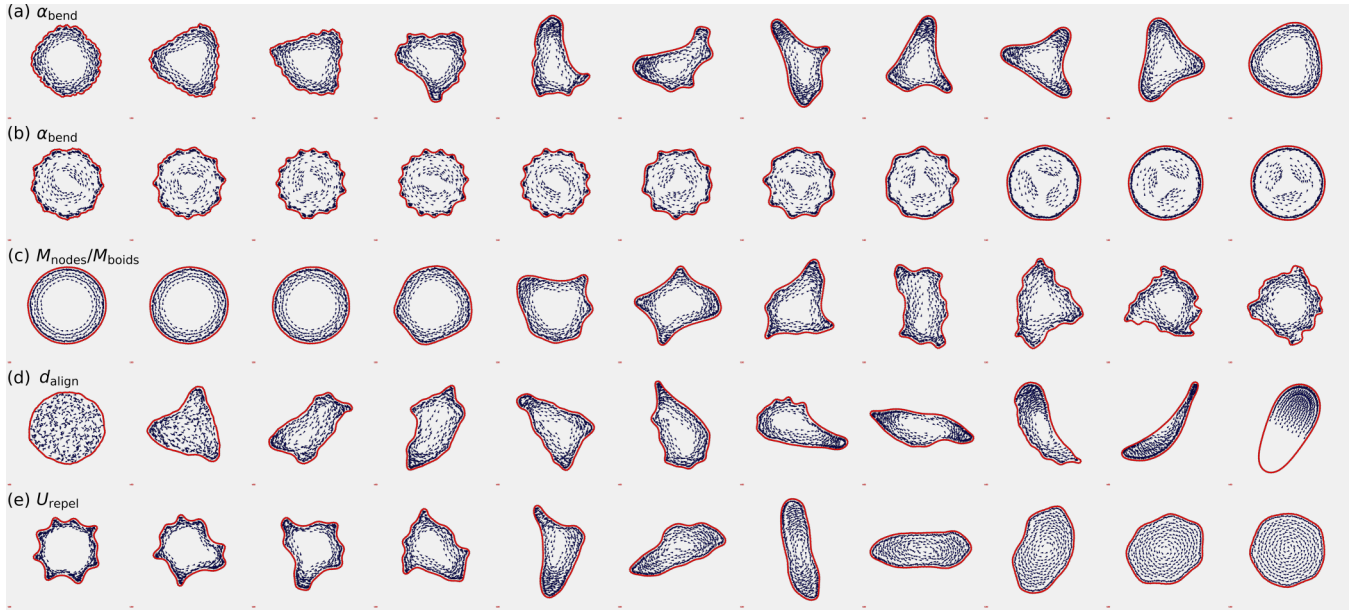


FIG. 1. Montages of snap shots showing series of simulations with parameters listed in Tables I and II. Each panel shows a single simulation snapshot. In each row, only a single simulation parameter is varied, keeping the rest constant. The varied parameter is printed on the top left of the row increases from left to the right. (a) Varying the stiffness of the boundary α_{bend} with a low value of boid repel distance d_{repel} . Softer boundaries have smaller wavelength corrugations. (b) Varying the stiffness of the boundary α_{bend} with a higher value of the repel distance, d_{repel} . (c) Varying the boundary to boid mass ratio, $M_{\text{nodes}}/M_{\text{boids}}$. Higher mass boundaries show smaller wavelength corrugations. (d) Varying the alignment distance d_{align} . A gaseous state is seen in the leftmost snapshot and a solidlike or jammed bullet state is seen on the far right. (e) Varying the repulsion strength U_{repel} .

consecutively increased in each simulation. Common parameters for these simulations are listed in Table I. Additional parameters for the series of simulations are listed in Table II. These series have been done with $N_{\text{boids}} = 400$; however, we saw similar phenomena with $N_{\text{boids}} = 100, 200$, and 800 . A live animation showing a circulating state can be seen in Ref. [40]. This animation is part of the first series of simulations and has bending moment $\alpha_{\text{bend}}/(M_{\text{boids}}v_0^2R) = 10^{-3}$. The fifth panel (from the left) in Fig. 1(a), the seventh panels in Figs. 1(c) and 1(d), and the fourth panel in Fig. 1(e) all have parameters approximately the same as this animation.

We first describe the different types of boid and boundary behaviors seen in our simulations. In Sec. III A, we discuss divisions in parameter space that separate gaseous, circulating, and jammed states. In Sec. III B, we discuss the sensitivity of boundary morphology to simulation parameters. Finally, in Sec. III C, we discuss the nature of the instability that causes the boundary to be ruffled or corrugated.

We see three types of collective phenomena: a disordered gaseous state, a solid-like state, and rotating or circulating states.

TABLE II. Simulation series.

Varying	Bending moment	Bending moment	Boundary mass	Align distance	Repel strength	Align+repel distances	Align distance, Boundary mass	Align distance, boid number
Figure	1(a)	1(b)	1(c)	1(d)	1(e)	2(a)	2(b)	2(c)
Factor	1.7	1.7	1.5	1.6	1.5	–	–	–
$\alpha_{\text{bend}}/(M_{\text{boids}}v_0^2R)$	$[10^{-4}, 0.01]$	$[10^{-4}, 0.01]$	10^{-3}	10^{-3}	10^{-3}	10^{-3}	10^{-3}	10^{-3}
$M_{\text{nodes}}/M_{\text{boids}}$	10	10	[1,57]	10	10	10	[1,32]	10
d_{align}/R	0.2	0.2	0.2	[0.01,1.1]	0.2	[0.01,3.3]	[0.01,3.3]	[0.01,1.3]
U_{repel}/v_0^2	0.1	0.1	0.1	0.1	[0.03,1.6]	0.1	0.1	0.1
d_{repel}/R	0.1	0.35	0.1	0.1	0.1	[0.04,0.4]	0.1	$0.1\sqrt{\frac{N_{\text{boids}}}{400}}$
N_{boids}	400	400	400	400	400	400	400	[100,800]
Initial conditions	Rotating	Rotating	Rotating	Not rotating	Rotating	Not rotating	Not rotating	Not rotating

The first row gives the parameter or parameters varied for the series. Each column gives parameters for simulations that are shown in the figure listed in the second row of the table. Additional parameters for these simulations are listed in Table I. Numbers in brackets give the range for the parameter that is varied. The third row, labeled ‘‘Factor,’’ gives the multiplicative factor used to increase the varied parameter for each consecutive simulation in Fig. 1.

In the disordered gaseous state, boids are not aligned with each other, there is little circulation or rotation, and the boid velocity dispersion is high. This state is characterized by a weak or short-range alignment force. An example of this state is in the leftmost panel of Fig. 1(d). This particular simulation has a very short alignment distance, $d_{\text{align}} = 0.01R$. Numerically, we find that $d_{\text{align}}\alpha_{\text{align}}/v_0 \lesssim 0.01$ gives a gaseous state. Contrary to the classic polar self-propelled particles [4,30,32,36], our boids exhibit a disordered state without stochastic perturbations. However, billiards within in a non-round but convex boundary can be chaotic [41]. Even if our boundary was smooth instead of composed of discrete nodes, ergodic behavior can be introduced via boids reflecting off the boundary. Ergodic behavior would also be introduced by the interboid repulsion due to frequent interactions between confined particles.

In the solid-like jammed bullet state, all boids are moving in the same direction. Boid positions and velocities appear frozen in a frame moving with along with them. The boid velocity dispersion is low and boids do not move relative to each other. This state is characterized by a strong or long-range alignment force and a lower mass boundary that is easily pushed by the boids. A low damping rate on the boundary aids in forming this state. An example of this state is in the rightmost panel of Fig. 1(d) (fourth panel from top) with $d_{\text{align}}/R = 1.1$. Numerically, we find that this state is likely when $d_{\text{align}}\alpha_{\text{align}}/v_0 \gtrsim 1$. Even though our simulations lack an interboid attractive force, confinement caused by the boundary can cause a jammed state. This state is similar to the jammed state seen previously in simulations of confined soft repelling self-propelled particles at high density [33]. These simulations also lack an alignment force; however, their boundary was rigid instead of flexible. The jammed state is perhaps also similar to moving cohesive groups or droplet states seen in simulations of unconfined unipolar self-propelled particles that attract each other (e.g., Refs. [32,36]).

Lastly, in the rotating or circulating states, the boids are circulating within the boundary. The boundary can be rotating but is usually moving more slowly than the boids, which all circulate in the same direction. The boundary shape can be circular, oval, irregular, or sprocket shaped. Oval loop-shaped flexible boundaries were previously seen in simulations of nonaligning self-propelled particles [23,25]. We use the word “sprocket” rather than “gear” or “ratchet” to describe states with more than a few radial projections.

For the irregular and sprocket shapes, the boundary is deformed by groups of boids. As the boids circulate, bulges in the boundary travel along the boundary. Irregular or sprocket boundaries are more likely if the boundary mass exceeds the total boid mass but the boundary is not so massive that the boids cannot push it. Irregular or sprocket boundaries are more likely with a more flexible rather than stiff boundary. As is true for the bullet states, the circulating states arise in the absence of interboid attraction. The confining boundary serves in place of attractive forces that cause circulating states in unconfined self-propelled particles (e.g., Ref. [32]). Because there is no attraction force between boids, we do not see multiple separate flocks, though we do see clumps of boids in divots or pockets moving along the boundary.

Long-lived states can depend on the initial boid velocity distribution. When alignment is strong and the boundary is lower mass, initially rotating boids are less likely to go into the bullet state. Once a system goes into a bullet state, we find that it stays there. Circulating states can nevertheless be long lived and even after long integrations, with integration time $t_{\text{max}} > 100t_R$, the simulation will not fall into a bullet state even if a different initial velocity distribution would put the system in such a state. Here $t_R = R/v_0$ is the time it takes a boid to travel the boundary radius (see the Appendix, Subsec. A 2).

The most interesting of the states seen in our simulations are those where the boundary becomes corrugated. Sokolov *et al.* [17] and DiLeonardo *et al.* [42] describe an asymmetric, rigid, nanofabricated gear that is spun by bacteria. In contrast, here we find that a flexible loop-shaped boundary can become corrugated and the corrugations can rotate because of unipolar self-propelled particles that are moving within the boundary. We could be seeing a modulational instability due to swim pressure inhomogeneities near the boundary that was predicted for nonaligning self-propelled particles [22].

Increased boid density near the boundary (bordertaxis) is particularly noticeable in the simulation with higher repel distance d_{repel} [see Fig. 1(b)]. The interplay of self-propulsion, confinement, and stochastic processes is often sufficient to explain accumulation of self-propelled particles on or near a boundary [23–25,43–46]. Here we lack stochastic perturbations; however boundary-boid and boid-boid interactions serve as a source of chaotic behavior that might aid in increasing the boid density near the boundary via diffusive-like behavior. Booids on the boundary only feel repulsion from other booids on one side, allowing them to be closer together than booids in the interior.

A. Phase diagrams

In Fig. 2, we show phase plots delineating gaseous, circulating, and bullet states. Figure 2(a) shows phases as a function of repel and alignment distances, d_{repel} and d_{align} . Figure 2(b) shows phases as a function of total boundary to boid mass ratio and the align distance and Fig. 2(c) shows phases as a function of the number of booids and the align distance. For this last figure, we set $d_{\text{repel}} \propto \sqrt{N_{\text{booids}}}$ so that the repel distance divided by mean boid number density remains constant in the different simulations. Otherwise, the high number density simulations would be at high pressure as boid repulsion would be pushing them up against the boundary.

The parameters for the simulations shown in Fig. 2 are listed in Table I and in the rightmost columns in Table II. In Fig. 2, red circles represent simulations giving gaseous states, green triangles represent those giving circulating states, and blue squares are simulations that ended in bullet states. Classification for this plot was done by eye from simulations run in the browser. We have shaded the different regions to show the locations of the different phases.

The transition between circulating and gaseous states is primarily sensitive to the align force and the boid density. The gas/circulating phases’ dividing line in Fig. 2(c) has slope consistent with alignment distance proportional to the mean distance between booids; $d_{\text{align}} \propto 1/\sqrt{N_{\text{booids}}}$. If the boid

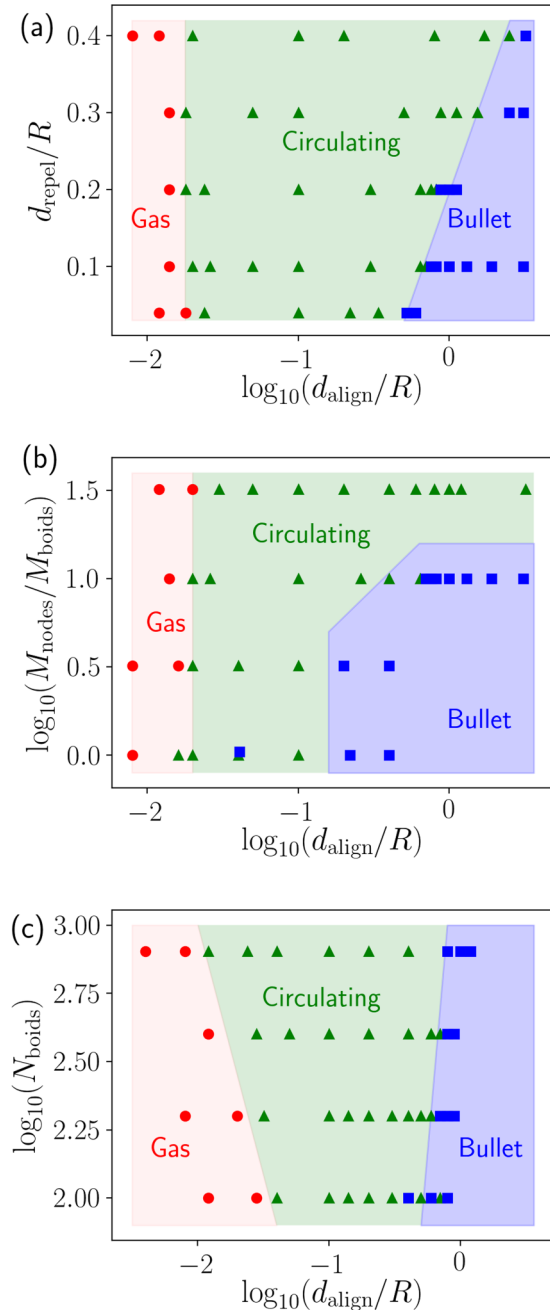


FIG. 2. Dependence of the type of collective motion on alignment distance and other parameters. (a) Phases are plotted as a function of the repel and align distances. (b) Phases as a function of the ratio of boundary and boid mass and the align distance. (c) Phases as a function of the number of boids and the align distance. Red circles represent simulations of gaseous states, green triangles are circulating states, and blue squares are those that ended in jammed or bullet states. We have roughly shaded the different regions. The jammed bullet phase is present when the alignment is strong, whereas the gaseous state is present when the alignment is weak. Circulating states lie in between the gaseous and bullet states. The simulations used to make this figure have parameters listed in Table I and the rightmost columns of Table II.

density is higher, a smaller alignment distance allows them to circulate.

The transition line between bullet and circulating states is sensitive to a number of parameters. More flexible, less damped, and lower mass boundaries are more likely to elongate and trap boids, aiding in formation of a jammed state. Confined self-propelled soft particles at high density jam [33], and unconfined self-propelled particle with strong cohesion can form moving solidlike droplets [32,36]. The sensitivity of the bullet/circulating phase line to bending moment α_{bend} , damping parameter γ_{damp} , and mass ratio $M_{\text{nodes}}/M_{\text{boid}}$ would be consistent with a picture where strong alignment pushes the boids into the boundary, increasing their density, but where the jammed state is only maintained when the boundary can fold and trap them.

B. Sensitivity of boundary corrugations on simulation parameters

We discuss the five series of simulations shown in Fig. 1 and with parameters listed in Tables I and II. In Fig. 1(a) (top panel), we show a series of simulations, all with the same parameters except that bending moment α_{bend} increases from simulation to simulation. The factors used to increase the varied parameter in each series are also listed in Table II. For example, the varied parameter for Fig. 1(a) is computed as follows: The lowest value of $\alpha_{\text{bend}}/(M_{\text{boids}}v_0^2R)$ in the first series is 10^{-4} . The factor used to vary this parameter is 1.7. The i th simulation has bending moment $\alpha_{\text{bend}}/(M_{\text{boids}}v_0^2R) = 10^{-4} \times (1.7)^{i-1}$. This set of simulations has $d_{\text{repel}} = 0.1$ and so has a short-range repulsive force. With a very flexible boundary [on the left in Fig. 1(a)] and small α_{bend} , the boundary has many corrugations. As the bending moment increases, the wavelength of the boundary corrugations increases.

The second series of simulations shown in Fig. 1(b) is similar to the first series except the repel distance $d_{\text{repel}} = 0.35$ is larger. The repel distance is large enough that boids are pushed against the boundary by their repulsion alone. This differs from the simulations at lower d_{repel} , where only the centrifugal force due to their circulation pushes them up against the boundary. Despite being in a different regime, we also see boundary corrugations in the series shown in Fig. 1(b), and again with wavelength increasing with increasing bending moment. In this regime, a single angular Fourier mode often dominates, whereas at lower repel distance d_{repel} the boundary corrugations were more irregular. With higher d_{repel} and lower bending moment α_{bend} , the boundary looks like a sprocket or a gear.

We were most surprised by the third series of simulations, shown in Fig. 1(c). In this series of simulations, the boundary mass is increased, with low-mass boundaries on the left and high-mass boundaries on the right. We had expected that a lower mass boundary would show more corrugations because it would be easier for the boids to push the boundary. However, we find that the opposite is true; the higher mass boundaries have boundaries with more corrugations.

In the fourth series, Fig. 1(d), we vary the alignment distance d_{align} . This set of simulations shows the transition from a gaslike state, at low d_{align} on the left to the jammed bullet-like state at high d_{align} , on the right. In some of the intermediate simulations, we saw a circulating flock of boids

that moved back and forth from one side of a boundary to the other.

Finally, in the fifth series, Fig. 1(e), we vary the repel force strength U_{repel} . This parameter affects the boid density. We find that the boundary is more likely to be corrugated when the boid density is higher near the boundary and at lower repel strength, U_{repel} .

C. Instability on the boundary

The most interesting phenomena illustrated by our dynamical system is corrugations in the boundary that grew during the simulations. The dynamics of the boundary is coupled to the collective motions. In this section, we examine the nature of the instability leading to the growth of corrugations on the boundary.

Hydrodynamic analogies for our boundary corrugations include ripples excited on a flag by wind, or the Kelvin-Helmholtz instability which is driven by the velocity difference across an interface between two fluids. Classically, instabilities can be studied by linearizing equations of motion and deriving a dispersion relation for wavelike solutions. The dispersion relation relates a the frequency of oscillation to a wave vector. Frequencies that have complex parts when the wave vectors are real correspond to wavelengths that are unstable to amplitude growth.

Using dynamic Euler-Bernoulli theory, the wave equation for a linear elastic beam under tension and with an applied force

$$\mu \frac{\partial^2 w}{\partial t^2} = -\alpha_{\text{bend}} \frac{\partial^4 w}{\partial x^4} + T \frac{\partial^2 w}{\partial x^2} + p(x), \quad (21)$$

where, as previously, $w(x)$ is beam displacement, α_{bend} is the bending moment or flexural rigidity, μ is the beam's linear mass density, and $p(x)$ is an applied force per unit length. We can use this equation to model the dynamics of our flexible boundary. Here the horizontal coordinate x is a plane parallel approximation to $R\theta$ in polar coordinates along the boundary with periodic boundary conditions and $w(x)$ is a radial displacement of the boundary away from its rest, circular state. The linear mass density in the boundary $\mu = M_{\text{nodes}}/(2\pi R)$. In Eq. (21), we have included a term dependent upon tension T , the longitudinal tension in the boundary. We estimate a mean value for the tension using Eq. (A7), $T \sim M_{\text{boids}} v_0^2/(2\pi R)$, and depending upon the total boid mass and associated pressure. The applied force $p(x)$ is due to boids pushing up against the boundary. We refer to this applied force as ‘‘swim pressure’’ (following Refs. [22,27,28]) or ‘‘boid pressure.’’

A perturbative solution of Eq. (21) with displacement $w(x, t) \propto e^{i(\omega t - kx)}$, frequency ω , and wave vector $k = 2\pi/\lambda$, for wavelength λ , and with applied pressure $p = 0$, gives a dispersion relation

$$\omega^2 = \frac{\alpha_{\text{bend}}}{\mu} k^4 + \frac{T}{\mu} k^2. \quad (22)$$

The tension-related k^2 and bending-rigidity-related k^4 terms are consistent with discussion on active particle mediated boundary instability in Ref. [22].

If the boids are moving parallel to a straight surface, they will not interact with the boundary. However, if they are moving next to a curved surface, their trajectories must curve. The pressure on the boundary due to the boids depends on the curvature of the boundary and the boid density $p_{\text{swim}} \propto \rho_{\text{boid}} \frac{\partial^2 w}{\partial x^2}$. The pressure force is opposite that due to tension in the boundary, as it would push in the same direction as a bulge in the boundary, rather than counter it. In this sense, the boid swim pressure acts like pressure variations in an incompressible fluid near a boundary that is derived from linearization of Bernoulli's equation. We estimate the pressure on the boundary

$$p_{\text{swim}} \sim -\beta_{\text{swim}} M_{\text{boid}} \frac{v_0^2}{2\pi R} \frac{\partial^2 w}{\partial x^2} \sim -\beta_{\text{swim}} T \frac{\partial^2 w}{\partial x^2}, \quad (23)$$

where β_{swim} is a dimensionless factor that we can adjust. This gives a simple approximate model for variations in boid pressure exerted along a corrugated boundary and is in a similar form to that predicted in Eq. (27) by Nikola *et al.* [22]. This form for the swim pressure gives a term in the wave equation similar to the tension term [see Eq. (A7) for tension] but with the opposite sign (and this is also consistent with the discussion in Ref. [22] supplements). The dispersion relation [in Eq. (22)] becomes

$$\omega^2 = \frac{\alpha_{\text{bend}}}{\mu} k^4 + \frac{T(1 - \beta_{\text{swim}})}{\mu} k^2. \quad (24)$$

In Fig. 3, we have plotted the phase velocity $\omega/(kv_0)$, computed using Eq. (24), as a function of wavelength for different boundary to boid mass ratios, bending moments, and two different values for the dimensionless coefficient β_{swim} . The values of boundary to total boid mass ratio and bending moments are the same as used in our simulation series. In Fig. 3(a), velocities are shown for $\beta_{\text{swim}} = 0$. This would be if the boids locally did not exert much pressure on the boundary that is above or below a mean value. In Fig. 3(b), velocities are shown for $\beta_{\text{swim}} = 0.8$. Orange solid, red dot-dashed, and maroon solid lines of increasing thickness have mass ratio $M_{\text{nodes}}/M_{\text{boids}} = 3, 10, 25$, respectively, and bending moment $\alpha_{\text{bend}}/(M_{\text{boids}} v_0^2 R) = 10^{-3}$. Thin cyan and thick blue dotted lines have $\alpha_{\text{bend}}/(M_{\text{boids}} v_0^2 R) = 10^{-2}$ and 10^{-4} , respectively, and mass ratio $M_{\text{nodes}}/M_{\text{boids}} = 10$. We note that the phase velocities shown in Fig. 3(b) do not reach zero. We suspect that instability is not caused by large β_{swim} , which would give a negative right-hand side to Eq. (24) and complex values for frequency ω . In this sense, our estimates for the phase velocity do not support the model for boundary instability explored in Ref. [22].

Figure 3 illustrates that higher boundary mass gives lower wave velocity on the boundary. Likewise, weaker boundaries (with lower α_{bend}) have lower wave velocity. The trends we see in Fig. 1, showing that corrugation wavelengths decrease with increasing boundary mass and decreasing bending moment, are matched by the trends we see in wave velocity. This suggests that the instability on the boundary grows when the wave speed on the boundary is similar to boid speed. Horizontal gray lines on Fig. 3(b) show constant velocities. Wavelengths to the right of where the curved lines cross a horizontal gray line have phase velocity below the value of the horizontal line. If instability depends on matching boid

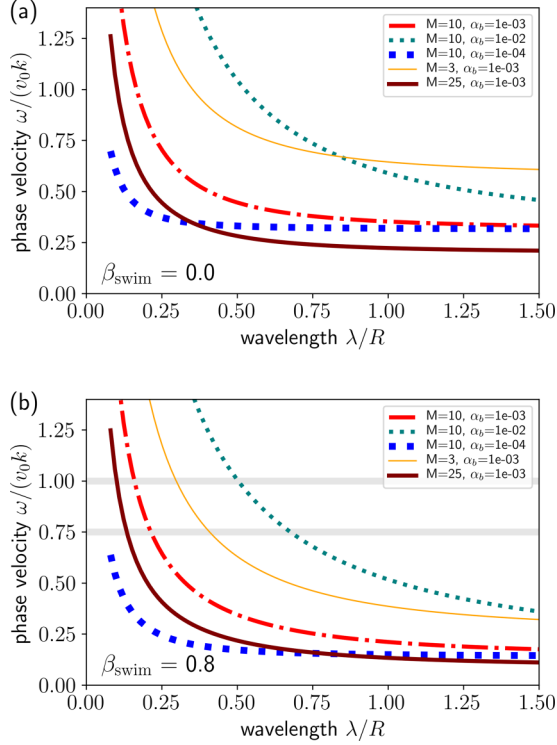


FIG. 3. Phase velocities for waves on the boundary for a simple model that takes into account swim pressure from boids. These were computed using the dispersion relation in Eq. (24). (a) No local boid swim pressure on the boundary. (b) Local solid swim pressure set by $\beta_{\text{swim}} = 0.8$. In both plots, orange solid, red dot-dashed, and maroon solid lines of increasing thickness have mass ratio $M_{\text{nodes}}/M_{\text{boids}} = 3, 10, 25$, respectively, and bending moment $\alpha_{\text{bend}}/(M_{\text{boids}}v_0^2R) = 10^{-3}$. Thin cyan and thick blue dotted lines have $\alpha_{\text{bend}}/(M_{\text{boids}}v_0^2R) = 10^{-2}$ and 10^{-4} , respectively, and mass ratio $M_{\text{nodes}}/M_{\text{boids}} = 10$. Horizontal gray lines are at velocity v_0 and $3/4v_0$. Wavelengths to the right of where the curved lines cross a horizontal line have phase velocity below the value of the horizontal line. If instability depends on matching boid speed to the velocity of waves on the boundary, then smaller wavelengths are unstable for higher mass and more flexible boundaries.

speed to the velocity of waves on the boundary, then smaller wavelengths are unstable with higher mass and more flexible boundaries.

Using our dispersion relation in Eq. (24), the wave vector that gives $\omega = kv_0$ (and matching wave phase velocity to boid speed) is

$$k_{\text{crit}} = \sqrt{\frac{\mu v_0^2 - T(1 - \beta_{\text{swim}})}{\alpha_{\text{bend}}}}. \quad (25)$$

The regime giving us interesting boundary morphology has $M_{\text{nodes}} > M_{\text{boids}}$ and critical wave vector

$$k_{\text{crit}}R \approx \sqrt{\frac{Rv_0^2M_{\text{boids}}}{2\pi\alpha_{\text{bend}}}} \sqrt{\frac{M_{\text{nodes}}}{M_{\text{boids}}}}, \quad (26)$$

where we have neglected β_{swim} . In terms of a critical wavelength $\lambda_{\text{crit}} = 2\pi/k_{\text{crit}}$,

$$\frac{\lambda_{\text{crit}}}{R} \approx 0.16 \left(\frac{\alpha_{\text{bend}}}{10^{-3}M_{\text{boids}}Rv_0^2} \right)^{\frac{1}{2}} \left(\frac{10}{M_{\text{nodes}}/M_{\text{boids}}} \right)^{\frac{1}{2}}. \quad (27)$$

The scaling and approximate values for the critical wavelength are consistent with the wavelengths giving phase velocity of v_0 shown in Fig. 3.

As long as the coefficient giving swim pressure strength $\beta_{\text{swim}} < 1$, the dispersion relation in Eq. (24) always gives real frequencies ω when the wave vectors are real. Only wavelike solutions would be present and perturbations on the boundary would not grow. If the dispersion relation has regions where frequency ω is complex for real k , then perturbations at these wavelengths would grow exponentially giving instability on the boundary. If the k^2 term in the dispersion is negative, then there is an instability at small wavelengths. This is the setting discussed by Nikola *et al.* [22] for instability of a filament embedded in a medium containing self-propelled particles. A modified form for the swim pressure might give a larger negative term in the dispersion relation and show instability.

Using a linearized version of Bernoulli's equation, a two-dimensional incompressible fluid approximation for boids moving at v_0 would give boid pressure perturbation with amplitude $p_k \propto M_{\text{boids}}(\omega - kv_0)^2/k$ for a perturbation $\propto e^{i(\omega t - kx)}$ on the boundary. However, unstable regions in the dispersion relation then occur at larger wavelengths for heavier boundaries, which is opposite to what is seen in our simulations [see Fig. 1(c)]. A model where swim pressure is proportional to boid density and boid density is proportional to the local boundary curvature (e.g., Ref. [44]) also would predict this trend that is *not* consistent with our simulations. If the local swim pressure is large and $\beta_{\text{swim}} > 1$ in Eq. (24), unstable regions would also give this incorrect trend. These types of instability models also predict rapid growth rates for the instability, also in contradiction to what we see in the simulations, where corrugations in the boundary take 5 to 10 crossing times t_R to grow.

The models discussed in the previous paragraph and Eq. (23) (and in Ref. [22]) have boid swim pressure perturbations, exerted on the boundary, that are in phase with the boundary perturbation. However, we see a difference in the boid motions between leeward and windward sides of corrugations in our simulations. This is most extreme for the massive boundaries on the right-hand side of Fig. 1(c) (third row), where boids are pushed outward toward the center of the enclosed region after they pass a convex region of the boundary. The difference between leeward and windward sides in the boid motions implies there is an asymmetry in the response of the boids to perturbations in the boundary. The response of the boids slightly lags behind the perturbation, giving a phase shift in the pressure response.

We consider a model where the boid swim pressure is slightly out of phase with a small perturbation on the boundary. For a perturbation $\propto e^{i(\omega t - kx)}$ on the boundary, we assume that the sign of the phase shift depends on $\bar{v} - \omega/k$, where \bar{v} is the mean speed of boids that are next to the boundary. We approximate $\bar{v} \sim v_0$ even though the mean speed \bar{v} is usually lower than v_0 because the boids are slowed by bouncing

against the boundary. The phase shift gives an additional complex component to the amplitude of the boid pressure perturbation $p_{\text{swim},k}$. We assume that the phase shift in boid pressure is in the same form as Eq. (23), contributing a complex component

$$\text{Im}(p_{\text{swim},k}) = i\delta_{\text{lag}}Tk^2\text{sign}(kv_0 - \omega) \quad (28)$$

to the swim pressure perturbation amplitude. Here δ_{lag} is a small dimensionless parameter describing the size of the lag.

Modifying Eq. (24), the resulting dispersion relation is

$$\omega^2 = \frac{\alpha_{\text{bend}}}{\mu}k^4 + \frac{T}{\mu}k^2[1 - \beta_{\text{swim}} + i\delta_{\text{lag}}\text{sign}(kv_0 - \omega)]. \quad (29)$$

Assuming that the parameter δ_{lag} is small, we find that the perturbation only grows if the imaginary term on the right-hand side is positive. An instability is present if $v_0 > \omega/k$, so only boundaries with slow wave speeds would be unstable to the growth of corrugations. As heavier boundaries have slower bending wave speeds, the delay would account for the relation between corrugation and boundary mass we see in Fig. 1(c).

With small δ_{lag} , we estimate an instability growth rate from the imaginary component of the frequency

$$\gamma(k) = \text{Im}(\omega) \approx \frac{\delta_{\text{lag}}Tk^2}{2\mu\text{Re}[\omega(k)]}. \quad (30)$$

Unstable perturbations would have amplitudes that increase exponentially with time, $\propto e^{\gamma(k)t}$. While all wavelengths larger than the critical one λ_{crit} (where wave speed matches boid speed) would be unstable (due to the sign of the phase lag), the growth rate is maximum near the smallest unstable wavelength, which is the critical one. Using Eq. (26) for the critical wave vector, we estimate the the growth rate for this wavelength,

$$\begin{aligned} \gamma(k_{\text{crit}})t_R &\approx \frac{T\delta_{\text{lag}}}{2\mu v_0^2}k_{\text{crit}}R \approx \frac{\delta_{\text{lag}}}{2} \sqrt{\frac{Rv_0^2 M_{\text{boids}}}{2\pi\alpha_{\text{bend}}}} \sqrt{\frac{M_{\text{boids}}}{M_{\text{nodes}}}} \\ &\approx 2\delta_{\text{lag}} \left(\frac{10^{-3}M_{\text{boids}}Rv_0^2}{\alpha_{\text{bend}}} \right)^{\frac{1}{2}} \left(\frac{10}{M_{\text{nodes}}/M_{\text{boids}}} \right)^{\frac{1}{2}}. \end{aligned} \quad (31)$$

We can test this phase-lag instability model by examining the rate that boundary perturbations grow in our simulations. In five simulations, we measure Fourier amplitudes $A_m(t) > 0$ as a function of time, where integer m gives the angular frequency of radius $R(\theta, t) = \sum_m A_m(t) \cos[m\theta + \phi_m(t)]$ as a function of angle θ along the boundary. For example, a triangular perturbation gives an amplitude A_3 . The angle ϕ_3 determines the orientation of the triangular perturbation. The five simulations have parameters taken from Tables I and II but with the boundary to boid mass ratio and bending moments chosen to be the same as the phase velocities plotted in Fig. 3. These simulations are the part of the first and third series listed in Table II and shown in the first and third rows of Fig. 1. In Fig. 4(a), we plot $\ln(\sum_{m=3}^7 A_m/R)$ as a function of time and in Fig. 4(b) we plot $\ln(\sum_{m=10}^{20} A_m/R)$. Lines have the same colors and styles as in Fig. 3.

Figure 4 shows that corrugation growth rates are faster with lower values of bending moment (comparing blue dotted, red dot-dashed, and thin teal dotted lines), as expected from

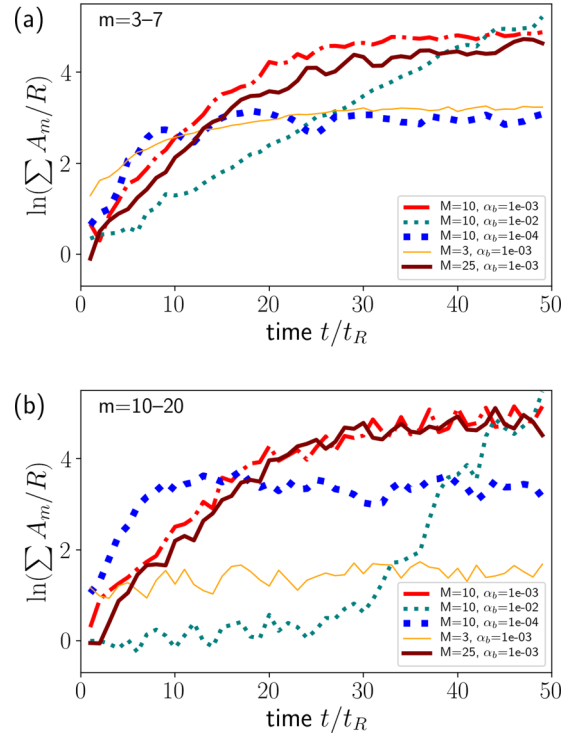


FIG. 4. The log of a sum of Fourier amplitudes measured from the boundary for five different simulations. (a) Using the $m = 3$ to 7 Fourier amplitudes. (b) Using the $m = 10$ to 20 amplitudes. The lines types and parameter choices are the same as in Fig. 3. The simulations have parameters the same as the first and third series of simulations listed in Table II except they have specific boundary to boid mass ratios and bending moments that are shown in the legends.

Eq. (31). The inverse dependence of growth rate on boundary to total boid mass ratio is less evident, but the mass ratio varies by a factor of about 3 rather than 10 as for the bending moment. The low-mass boundary only grows larger wavelength perturbations (with lower Fourier index m) and the growth rate is slower than for the higher mass boundaries with the same bending moment (comparing thin orange to thick red and maroon lines). The trends we see in Fig. 4 are consistent with those predicted by Eq. (31).

We use our numerically measured growth rates to estimate the size of the pressure lag. In Eq. (31) we have estimated the growth rate of the critical wavelength for the mass ratio 10 and $\alpha_{\text{bend}}/(M_{\text{boids}}v_0^2R) = 10^{-3}$ simulation which is shown with a dot-dashed red line in Fig. 4. The slope of the red line gives a growth rate of $\gamma t_R \sim 0.2$. Equating this to the growth rate in Eq. (31), we estimate $\delta_{\text{lag}} \sim 0.1$. The required lag for the pressure is small enough to be consistent with the appearance of the simulations. This implies that a small delay in boid response moving over boundary perturbations can account for the instability on the boundary.

Throughout the discussion in this section, we have assumed that tension on the boundary was that estimated by Eq. (A7). However, if the boid separation is shorter than the repel distance, $\sqrt{\frac{\pi R^2}{N_{\text{boids}}}} < d_{\text{repel}}$, then there is additional tension on the boundary because the boids are pushed against the boundary by their repulsion. An increase in tension increases

the wave speed and would reduce the wavelength of corrugations on the boundary. The second series of simulations shown in Fig. 1(b) (second row) is in this regime and shows weaker boundary perturbations. Comparison of this simulation to that with identical parameters but lower repel distance d_{repel} [Fig. 1(a), top row] shows that the corrugations in the higher tension simulations tend to be shorter wavelength, confirming our expectation. A single Fourier perturbation tends to dominate in these simulations, but we lack an explanation for this phenomenon.

What accounts for the size of the phase lag parameter δ_{lag} ? The phase lag may be due to the time it takes other boids to push near-boundary boids back onto the boundary. This time might be governed by the strength of the interboid repel force. We have noticed that a weaker repel force U_{repel} gives larger density contrasts in the boids. We would expect this to give a larger asymmetry between windward and leeward sides of corrugations in the boid distribution, leading to faster corrugation growth rates and larger amplitude corrugations but not necessarily a change in the wavelengths that are unstable. However, in Fig. 1(e) (fifth row), the simulations with lower U_{repel} do seem to have smaller wavelength corrugations and with larger U_{repel} , the boundary instability is suppressed. The variation in the wavelengths of instability must be due to another cause, perhaps because changing U_{repel} also affects boid density near the boundary and the pressure-related tension on the boundary, which in turn affects the speed of boundary waves. Booids are slowed down near the boundary and if the mean speed depends on U_{repel} , this too could affect the wavelengths that are unstable. We lack a straightforward way to predict the delay parameter, δ_{lag} . Better understanding of the boid's continuum dynamics near the boundary may make it possible to predict the phase lag from the repel force law and mean boid number density.

In summary, we have explored simple models for boid swim pressure, exerted onto the boundary, that would give instability on the boundary. A model with boid swim pressure dependent on the boundary curvature and slightly lagging its corrugations is most successful at matching sensitivity of boundary corrugation wavelength to boundary mass, bending moment, and the corrugation growth rates. Perturbations on the boundary that move with wave speed slower than but near the boid speed are most likely to grow and this determines the wavelengths that grow on the boundary.

IV. SUMMARY AND DISCUSSION

We have carried out a numerical exploration in two dimensions of self-propelled particles with alignment and repelling forces that are enclosed in a flexible elastic loop. We primarily find three types of long-lived states: a stochastic gaslike state, a solidlike or jammed bullet state where the booids align and push the boundary in a single direction, and rotating or circulating states. The gaseous and circulating states resemble those exhibited by unconfined unipolar self-propelled particles with cohesive or attractive interactions [4,32]. The solidlike state resembles the jammed state seen in simulations of confined soft repulsive self-propelled particles at high density [33] and the moving droplets seen in simulations of unconfined self-propelled particle with strong cohesion

[32,36]. We recover these three types of states without cohesion due to the confining nature of the boundary.

The most of interesting of the states exhibited by our simulations are the circulating states as they include rotating ovals and sprocket-shaped and irregular or ruffled boundaries. Oval-shaped boundaries are similar to those seen in simulations of nonaligning stochastically perturbed self-propelled particles [23,25]. The ruffled or sprocket-shaped rotated boundaries mimic the rotating ratchet that was achieved by placing a rigid ratchet in a solution of active particles [17,18,42], but here the collective motion of the self-propelled particles and instability on the boundary drive the rotation. The instability is likely mediated by boid pressure inhomogeneities, as predicted by Nikola *et al.* [22]. However, the instability is most noticeable in the simulations with more massive and flexible boundaries. The wavelength of corrugations on the boundary is near the wavelength of elastic waves on the boundary that have phase velocity equal to the particle swim speed. We suspect that the instability depends on a lag between boid swim pressure exerted on the boundary and boundary shape perturbations. In this sense, our instability model differs from the model in Ref. [22] that lacks a phase lag.

It may be possible to devise an experiment giving an instability on a flexible boundary that is mediated by active particles. Here we considered a uniform loop boundary, but a boundary could be designed to be more flexible in one region than another. For example, if the instability is fast, waves might be excited on one side of a loop, making it possible to fix the other side to another surface. States with rotating or fluttering boundaries might be used to generate fluid flow or vorticity or to create a swimmer. These artificial mechanisms could more efficiently use power from self-propelled particles as the particles are in proximity to the moving boundary rather than distributed in a solution, though providing the particles with an energy source for propulsion could be more difficult as their fuel must be stored within or cross the boundary.

In this study, we ignored stochastic perturbations and cohesion in the self-propelled particles and the hydrodynamics of the medium in which the self-propelled particles move. Phase diagrams for classes of DADAM tend to scale with the ratio of density to noise strength, with noisier systems more likely to display disordered phases [30]. Our simulations were restricted to a few hundred booids. Future studies could extend and vary the physical model and explore dynamics in three dimensions. Future work could also explore other types of active materials that are enclosed by flexible boundaries, such as active self-propelled rods (e.g., Refs. [47,48]) or active nematics (e.g., Refs. [30,49–52]). With unipolar self-propelled particles, we did not see long-lived bending oscillations. Perhaps other types of active materials enclosed in a flexible boundary could exhibit this type of phenomena.

ACKNOWLEDGMENTS

We thank Steve Teitel and Randal C. Nelson for helpful discussions. This material is based upon work supported in part by NASA Grant No. 80NSSC17K0771, National Science Foundation Grant No. PHY-1757062, and National Science Foundation Grant No. DMR-1809318.

APPENDIX: NUMERICAL IMPLEMENTATION

All boundary node masses are equivalent and all boid masses are equivalent; however, node mass is usually not equal to boid mass. The total number of boids and nodes remains fixed during the simulation. For visualization, we translate the viewing window so that it is centered on the center of mass of the boundary.

1. Initial conditions

The simulations are initialized with boids initially confined within a circle with radius of 0.9 the initial boundary radius, R . Booids are initially uniformly and randomly distributed within this circle. We explored two types of initial conditions for the booids, an initially rotating flock and a nearly stationary flock. In both cases, we also added a small initial random velocity, uniformly distributed in angle, of size $0.1 v_0$, where v_0 is the boid swim speed. The rotating swarm has booids initially rotating about the boundary center at a velocity of $0.8 v_0$. Circulating initial conditions are chosen when we study the circulating states, whereas random initial conditions without mean rotation are chosen when we study the transitions between gaseous-like, circulating, and jammed states.

The boundary nodes are initially placed in a circle of radius R , equally spaced and at zero velocity. Springs between neighboring nodes are initially set to their rest length and all springs have the same spring constant. The bending moment does not vary as a function of position on the boundary.

2. Units

We work in units of boid speed v_0 , initial boundary radius R , and total boid mass M_{booids} . A unit of time is

$$t_R \equiv R/v_0, \quad (\text{A1})$$

which is the time for a lone boid moving at v_0 to cross the radius R of the boundary. After choosing these units, the free parameters are the total boundary mass M_{nodes} which is also the boid to boundary mass ratio, the number of nodes and booids N_{nodes} and N_{booids} , the alignment force strength and length scale, α_{align} and d_{align} , the repel force strength and length scale U_{repel} and d_{repel} , the bending moment α_{bend} , the node damping parameter γ_{damp} , the node-boid interaction strength and length scale, F_{interact} and d_{interact} , and the spring constant k_s . To run a simulation, we also require a time step dt , which is fixed during the simulation, and a maximum length of time t_{max} to integrate. This is a large parameter space, but not all combinations of these parameters necessarily affect the collective dynamics or are in regimes that are physically interesting or could be realized numerically. As long as the number of nodes is high enough that the booids are confined and they smoothly interact with the boundary, the dynamics should not depend on the number of nodes in the boundary or the parameters describing the boid-node interactions. The springs are used to set the boundary length so the spring constant should not affect the dynamics. The dynamics could depend upon the number and mass of booids as the swim pressure, or pressure exerted by booids on the boundary, depends on their number density.

3. The time step

The speed of compression waves traveling in a linear mass-spring chain is

$$v_c = \sqrt{\frac{k_s}{m_{\text{node}}}} \Delta s = \sqrt{\frac{k_s}{m_{\text{node}}}} \frac{2\pi R}{N_{\text{nodes}}}. \quad (\text{A2})$$

For numerical stability, a CFL-like condition for the time step is that it must be less than the time it takes a compression wave to travel between nodes or

$$dt < \sqrt{\frac{m_{\text{node}}}{k_s}}. \quad (\text{A3})$$

In the continuum limit, Eq. (16) gives a dispersion relation for bending waves equivalent to that from Euler-Bernoulli beam theory

$$\omega^2 = \frac{\alpha_{\text{bend}}}{\mu} k^4, \quad (\text{A4})$$

where α_{bend} is the bending moment or flexural rigidity, $\mu = m_{\text{node}}/\Delta s$ is the linear mass density, ω is angular wave frequency, and k is the wave vector. The simulation time step should be chosen so that small corrugations in the boundary are not numerically unstable. Taking the wave speed for wave vector $k = 1/\Delta s$, from the node separation, a condition on the time step for numerical stability is

$$dt < \sqrt{\frac{m_{\text{node}}}{\alpha_{\text{bend}} \Delta s}} (\Delta s)^2. \quad (\text{A5})$$

The time step should be shorter than the time it takes a boid to travel between boundary nodes, the mean distance between booids, and the repel, align, and boundary interaction distances,

$$dt < \min \left(\frac{\Delta s}{v_0}, \frac{1}{v_0} \sqrt{\frac{\pi R^2}{N_{\text{booids}}}}, \frac{d_{\text{repel}}}{v_0}, \frac{d_{\text{align}}}{v_0}, \frac{d_{\text{interact}}}{v_0} \right). \quad (\text{A6})$$

We chose the time step to satisfy Eqs. (A3), (A5), and (A6), with Eq. (A5) usually being the most restrictive.

4. Tension in the boundary

The springs are present to keep the boundary length nearly constant. We would like the springs to be strong enough that the choice of spring constant does not affect the simulation collective behavior. Because they must turn, booids circulating near a circular boundary exert a pressure on the boundary. On average, the force per unit length on the boundary is $p \sim M_{\text{booids}} \frac{v_0^2}{R} \frac{1}{2\pi R}$. This pressure is balanced by a tension in the boundary (sometimes called wall tension and related to hoop stress) that depends on the curvature of the boundary, $p \sim T/R$. Balancing these two estimates, we estimate the tension on the boundary

$$T \sim M_{\text{booids}} \frac{v_0^2}{R} \frac{1}{2\pi}. \quad (\text{A7})$$

This tension can stretch each spring by δx from its rest length, giving tension $T = k_s \delta x$. The spring strain is $\epsilon = \delta x/\Delta s$ with spring rest length $\Delta s = 2\pi R/N_{\text{nodes}}$. Setting tension from wall strain equal to that from spring tension, we solve for the spring

strain to give a dimensionless parameter

$$\epsilon_{ks} \equiv \frac{M_{\text{boids}} v_0^2 N_{\text{nodes}}}{(2\pi R)^2 k_s}. \quad (\text{A8})$$

As long as this parameter is small, the springs should remain near their rest length and the choice of spring constant should not affect the behavior of the simulations. We ensure that our spring constant k_s is large enough that $\epsilon_{ks} < 1$ is satisfied.

5. Other constraints on parameters

The boundary-boid interaction should primarily cause boids to reflect off the boundary. The acceleration on the boids from the boundary nodes should exceed the interboid repel force

$$\frac{F_{\text{interact}}}{m_{\text{boid}}} \frac{d_{\text{interact}}}{\Delta s} \gtrsim \frac{U_{\text{repel}}}{d_{\text{repel}}}, \quad (\text{A9})$$

where the factor $d_{\text{interact}}/\Delta s$ describes the number of nodes that push away a single boid as it approaches the boundary. We also require internode distance to be similar to or less than the boundary interaction distance, $\Delta s \lesssim d_{\text{interact}} \ll R$. The interaction force should not be so large that boids on the boundary move a large distance during a single time step, giving an upper bound

$$\frac{F_{\text{interact}}}{m_{\text{boid}}} \frac{dt}{v_0} \lesssim 1. \quad (\text{A10})$$

We maintain these conditions so that the parameters describing the boid-node interaction force should not significantly affect the boid collective behavior. We have halved the time step and we doubled the spring constant to check that these did not affect our simulations. We repeated simulations to check that boid distribution and boundary morphologies look similar at the end. There is sensitivity to initial conditions with some simulations freezing or jamming in a bullet-like state and others with the same parameters remaining in a circulating state. This is discussed in more detail in Sec. III.

If the interboid alignment force is too weak, then many boid crossing travel times would be required for collective phenomena to develop. We maintain alignment

strength $\alpha_{\text{align}} t_R > 1$ so that self-propelled particles align on a timescale shorter than the travel time across the enclosed region. This condition also ensures that transient behavior decays within a few dozen domain travel times, t_R . Likewise, we keep the repel strength divided by the square of the swim speed U_{repel}/v_0^2 to be of order 1 so that the boids effectively repel one another during a simulation extending a few dozen crossing times t_R . There is some degeneracy between alignment strength α_{align} and distance d_{align} in how these parameters affect collective behavior as both affect boid alignment. There is also a degeneracy between repel strength U_{repel} and distance d_{repel} as both parameters determine interboid repulsion. Consequently we usually fix the alignment and repel strengths α_{align} and U_{repel} , and vary their length scales d_{align} and d_{repel} in our numerical exploration of collective phenomena.

The damping parameter γ_{damp} mimics friction or viscous interaction with a background substrate or fluid. If the damping parameter $\gamma_{\text{damp}} t_R \gg 1$, then the boundary is overdamped and will not be sensitive to boid pressure. If $\gamma_{\text{damp}} t_R$ is extremely small, then circulating boids within the boundary will cause the boundary to rotate, eventually matching the boid rotation speed. We set $\gamma_{\text{damp}} t_R = 0.1$, an intermediate value, so that transient behavior will decay within a few dozen crossing times.

To allow transient behavior to decay, we run each simulation for $t_{\text{max}} = 50t_R$. We show in Sec. III C that the growth of structure on the boundary usually saturates by this time.

6. Code repository

We checked our classification of collective behavior and phenomena with two independently written codes. One version is written in C, uses an OpenGL display, and nearest neighbor searches are accelerated with a 2D quad-tree search algorithm based on the Barnes-Hut algorithm [53]. This code can be found in Ref. [54]. Another version of our code is written in JAVASCRIPT using the p5.js library (see Ref. [55]). This code displays in a web browser and nearest-neighbor searches are not accelerated. This code is available on github in Ref. [56]. The figures in this paper were made with the JAVASCRIPT code.

-
- [1] C. W. Reynolds, in *Proceedings of the 14th Annual Conference on Computer Graphics and Interactive Techniques*, edited by M. C. Stone, SIGGRAPH '87 (ACM Press, New York, NY, 1987), Vol. 21, pp. 25–34.
- [2] T. Vicsek, A. Czirok, E. Ben-Jacob, I. Cohen, and O. Shochet, *Phys. Rev. Lett.* **75**, 1226 (1995).
- [3] J. Toner and Y. Tu, *Phys. Rev. Lett.* **75**, 4326 (1995).
- [4] H. Levine, W.-J. Rappel, and I. Cohen, *Phys. Rev. E* **63**, 017101 (2000).
- [5] W. F. Paxton, K. C. Kistler, C. C. Olmeda, A. Sen, S. K. St. Angelo, Y. Cao, T. E. Mallouk, P. E. Lammert, and V. H. Crespi, *J. Am. Chem. Soc.* **126**, 13424 (2004).
- [6] V. Narayan, S. Ramaswamy, and N. Menon, *Science* **317**, 105 (2007).
- [7] S. Thutupalli, R. Seemann, and S. Herminghaus, *New J. Phys.* **13**, 073021 (2011).
- [8] J. K. Parrish and L. Edelstein-Keshet, *Science* **284**, 99 (1999).
- [9] J. Deseigne, O. Dauchot, and H. Chaté, *Phys. Rev. Lett.* **105**, 098001 (2010).
- [10] J. Palacci, C. Cottin-Bizonne, C. Ybert, and L. Bocquet, *Phys. Rev. Lett.* **105**, 088304 (2010).
- [11] J. Palacci, S. Sacanna, A. Steinberg, D. Pine, and P. Chaikin, *Science* **339**, 936 (2013).
- [12] A. Bricard, J.-B. Caussin, N. Desreumaux, O. Dauchot, and D. Bartolo, *Nature (London)* **503**, 95 (2013).
- [13] J. P. Hernandez-Ortiz, C. G. Stoltz, and M. D. Graham, *Phys. Rev. Lett.* **95**, 204501 (2005).
- [14] A. Bricard, J.-B. Caussin, D. Das, C. Savoie, V. Chikkadi, K. Shitara, O. Chepizhko, F. Peruani, D. Saintillan, and D. Bartolo, *Nat. Commun.* **6**, 7470 (2015).

- [15] V. Petrolli, M. Le Goff, M. Tadrous, K. Martens, C. Allier, O. Mandula, L. Herve, S. Henkes, R. Sknepnek, T. Boudou *et al.*, *Phys. Rev. Lett.* **122**, 168101 (2019).
- [16] J. Harder, C. Valeriani, and A. Cacciuto, *Phys. Rev. E* **90**, 062312 (2014).
- [17] A. Sokolov, M. Apodaca, B. Grzybowski, and I. Aranson, *Proc. Natl. Acad. Sci. USA* **107**, 969 (2010).
- [18] L. Angelani, A. Costanzo, and R. D. Leonardo, *Europhys. Lett.* **96**, 68002 (2011).
- [19] Z. Gao, H. Li, X. Chen, and H. P. Zhang, *Lab Chip* **15**, 4555 (2015).
- [20] C. Bechinger, R. Di Leonardo, H. Lowen, C. Reichhardt, G. Volpe, and G. Volpe, *Rev. Mod. Phys.* **88**, 045006 (2016).
- [21] W.-D. Tian, Y. Gu, Y.-K. Gua, and K. Chen, *Chin. Phys. B* **26**, 100502 (2017).
- [22] N. Nikola, A. P. Solon, Y. Kafri, M. Kardar, J. Tailleur, and R. Voituriez, *Phys. Rev. Lett.* **117**, 098001 (2016).
- [23] M. Paoluzzi, R. D. Leonardo, M. Marchetti, and L. Angelani, *Sci. Rep.* **6**, 34146 (2016).
- [24] A. Deblais, T. Barois, T. Guerin, P. H. Delville, R. Vaudaine, J. S. Lintuvuori, J. F. Boudet, J. C. Baret, and H. Kellay, *Phys. Rev. Lett.* **120**, 188002 (2018).
- [25] C. Wang, Y.-K. Guo, W.-D. Tian, and K. Chen, *J. Chem. Phys.* **150**, 044907 (2019).
- [26] L. Angelani, R. Di Leonardo, and G. Ruocco, *Phys. Rev. Lett.* **102**, 048104 (2009).
- [27] S. C. Takatori, W. Yan, and J. F. Brady, *Phys. Rev. Lett.* **113**, 028103 (2014).
- [28] W. Yan and J. F. Brady, *J. Fluid Mech.* **785**, R1 (2015).
- [29] G. Junot, G. Briand, R. Ledesma-Alonso, and O. Dauchot, *Phys. Rev. Lett.* **119**, 028002 (2017).
- [30] H. Chaté and B. Mahault, [arXiv:1906.05542](https://arxiv.org/abs/1906.05542).
- [31] H. Chaté, F. Ginelli, G. Gregoire, F. Peruani, and F. Raynaud, *Eur. Phys. J. B* **64**, 451 (2008).
- [32] J. R. Touma, A. Shreim, and L. I. Klushin, *Phys. Rev. E* **81**, 066106 (2010).
- [33] S. Henkes, Y. Fily, and M. C. Marchetti, *Phys. Rev. E* **84**, 040301(R) (2011).
- [34] A. Costanzo and C. K. Hemelrijk, *J. Phys. D: Appl. Phys.* **51**, 134004 (2018).
- [35] B. ten Hagen, R. Wittkowski, D. Takagi, F. Kümmel, C. Bechinger, and H. Löwen, *J. Phys.: Condens. Matter* **27**, 194110 (2015).
- [36] G. Gregoire and H. Chaté, *Phys. Rev. Lett.* **92**, 025702 (2004).
- [37] M. Kass, A. A. Witkin, and D. Terzopoulos, *Int. J. Comp. Vision* **1**, 321 (1988).
- [38] M. Bergou, M. Wardetzky, S. Robinson, B. Audoly, and E. Grinspun, *ACM Trans. Grap.* **27**, 63 (2008).
- [39] J. Frouard, A. C. Quillen, M. Efroimsky, and D. Gianella, *Mon. Not. R. Astron. Soc.* **458**, 2890 (2016).
- [40] https://aquillen.github.io/boids_in_a_loop/
- [41] L. Bunimovich, *Commun. Math. Phys.* **65**, 295 (1979).
- [42] R. DiLeonardo, L. Angelani, D. Dell'Arciprete, G. Ruocco, V. Iebba, S. Schippa, M. P. Conte, F. Mecarini, F. D. Angelis, and E. D. Fabrizio, *Proc. Natl. Acad. Sci. USA* **107**, 9541 (2010).
- [43] J. Elgeti and G. Gompper, *Europhys. Lett.* **101**, 48003 (2013).
- [44] Y. Fily, A. Baskaran, and M. F. Hagan, *Soft Matter* **10**, 5609 (2014).
- [45] B. Ezhilan, R. Alonso-Matilla, and D. Saintillan, *J. Fluid Mech.* **781**, R4 (2015).
- [46] L. Caprini, B. Marini, and U. Marconi, *Soft Matter* **14**, 9044 (2018).
- [47] A. Kaiser, H. H. Wensink, and H. Löwen, *Phys. Rev. Lett.* **108**, 268307 (2012).
- [48] M. Bär, R. Grossmann, S. Heidenreich, and F. Peruani, *Annu. Rev. Condens. Matter Phys.* **11**, 441 (2019).
- [49] S. Ramaswamy, R. A. Simha, and J. Toner, *Europhys. Lett.* **62**, 196 (2003).
- [50] T. Sanchez, D. T. N. Chen, S. J. DeCamp, M. Heymann, and Z. Dogic, *Nature (London)* **401**, 431 (2012).
- [51] M. C. Marchetti, J. F. Joanny, S. Ramaswamy, T. B. Liverpool, J. Prost, M. Rao, and R. A. Simha, *Rev. Mod. Phys.* **85**, 1143 (2013).
- [52] S. P. Thampi, R. Golestanian, and J. M. Yeomans, *Europhys. Lett.* **105**, 18001 (2014).
- [53] J. Barnes and P. Hut, *Nature (London)* **324**, 446 (1986).
- [54] <https://github.com/jsmucker/boids-in-a-boundary>
- [55] <https://p5js.org/>
- [56] https://github.com/aquillen/boids_in_a_loop